Measuring the Magnetization from the Image of the Stripe Magnetic Domain

Kyoung-Woong Moon,[1] Jungbum Yoon,[1] Jun Woo Choi,[2] Changsoo Kim,[1] Dong-Ok Kim,[1] Dongseuk Kim,[1] Byong Sun Chun,[1] Byoung-Chul Min,[2] and Chanyong Hwang[1,*]

[1]*Spin Convergence Research Team, Korea Research Institute of Standards and Science, Daejeon 34113, Republic of Korea*

[2]*Center for Spintronics, Korea Institute of Science and Technology, Seoul 02792, Republic of Korea*

Magnetic imaging techniques visualize magnetization states in detail, including magnetization directions and magnetic domains. Generally, such imaging methods determine only the relative magnetization, while the absolute value of magnetization remains unknown. Measuring absolute magnetization requires the separate measurement of a reference material, but for samples with just a few ferromagnetic layers, these techniques can no longer be applied. We show a simple magneto-optical imaging method for obtaining the absolute value of magnetization using the parallel stripe domains formed by an electric current in thin films. The parallel stripes in the films consist of repeating up- and down-magnetized domains with a certain periodicity. In the absence of an external magnetic field, the normalized areas of up and down domains are equal. However, application of an external perpendicular magnetic field can change these normalized areas of each domain because the magnetic field prefers only one domain depending on the direction. Measuring these normalized areas and the stripe periodicity using conventional imaging techniques is sufficient to determine the absolute value of magnetization.

I. INTRODUCTION

The phenomena of stripe formation have drawn much attention for several decades [1,2]. The physics of stripe pattern formation has shown a universal behavior [3], with numerous phenomena [4–10] that appear to be different being describable by similar forms of the Hamiltonian including short-range attractive and long-range repulsive interactions. In magnetic films, stripe patterns are usually observed in the domain structure [11–19]. The repeated magnetization states prefer half-up and half-down magnetization to minimize the magnetic dipolar energy. The relationship between the periodicity and the energy minimization process based on magnetic parameters [12–14,18–23] has especially been studied. Recently, such stripe-domain states have drawn a lot of attention because stripe domains are a precursor of magnetic skyrmion states [11,16,17].

The most fundamental parameter of magnetic materials is magnetization, that is, the magnetic moment per unit volume, which is a vector quantity. Magnetic imaging techniques [24–30] visualize magnetization states in detail, including magnetization directions and magnetic domains. Generally, such imaging methods determine only the relative magnetization, while the absolute value

of magnetization remains unknown. Measuring absolute magnetization requires a separate measurement [31,32] such as vibrating sample magnetometer (VSM) or superconducting quantum interference device (SQUID). For samples with just a few atomic layers in depth or a few μm in lateral size, these techniques can no longer be applied since the magnetic flux from these small samples cannot reach the detection limit. In this paper, we show a simple magneto-optical imaging method for obtaining the absolute value of magnetization using the parallel stripe domains [12–14] formed by an electric current [17] in thin magnetic films.

II. PAPALLEL STRIPE DOMAIN STATE

A schematic of parallel stripe domains in a thin film with perpendicular magnetic anisotropy (PMA) is shown in Fig. 1(a). Because of the PMA, up domains ($+z$ magnetization, light gray) and down domains ($-z$ magnetization, dark gray) are repeated along the x direction with a repetition number N. Such magnetization states are extended in the y direction with length L and in the z direction with thickness d. Following the definitions used in Ref. [14], the structure parameters are: W, the width of one of the up or down domains, and λ, the periodicity of the up and down domains. Between the up and down domains, the magnetization rotates in space from either $+z$ or $-z$ toward the x-y plane, becomes purely in-plane at the rotation center,
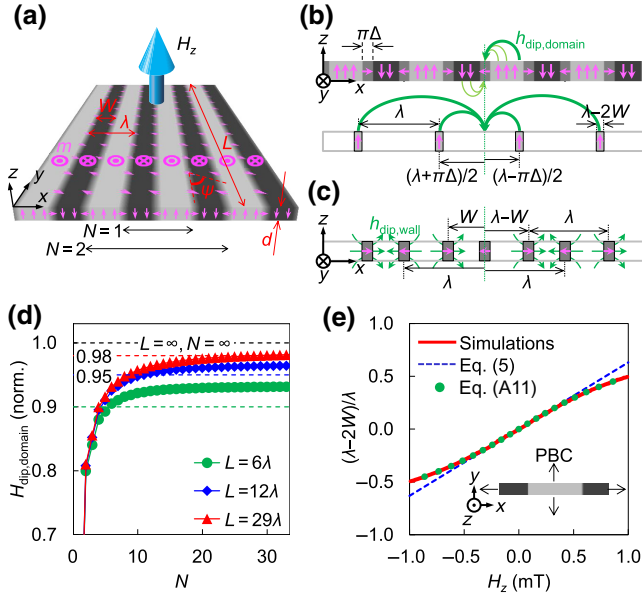
*cyhwang@kriss.re.kr

FIG. 1. Parallel stripe domains. (a) Schematic of stripe domains. Light (dark) gray indicates up (down) magnetization. Pink arrows represent magnetization vectors. (b) Cross section of stripe domains. Green arrows show the dipolar fields from the domains. The lower image represents the dipolar field produced by uncompensated parts of the up domains at the center of an arbitrary domain wall (dashed green line). (c) Dipolar fields generated by the domain walls. (d) Normalized $H_{\text{dip,domain}}$ as a function of N and L. (e) Simulation of $(\lambda - 2W)/\lambda$ $(=R)$ variation with respect to H_z. The inset shows the initial magnetization state for the simulation with the PBC.

and then rotates to either $-z$ or $+z$, respectively, starting a new domain. These x-y aligned bands form the magnetic domain walls, which are described by a normalized magnetization $\mathbf{m} = (m_x, m_y, m_z)$ when the wall center is $x = 0$ such as

$$m_x(x) = \sin(\psi)\text{sech}(x/\Delta), \quad (1)$$

$$m_y(x) = \cos(\psi)\text{sech}(x/\Delta), \quad (2)$$

$$m_z(x) = \tanh(x/\Delta), \quad (3)$$

where Δ is the domain wall width and ψ is the in-plane angle of the domain wall magnetization [13,14]. We assume that the domain walls have chirality [33–36], that is, the magnetization directions of the domain walls alternate such that each is antiparallel to that of the nearest neighboring domain wall on either side [Fig. 1(a)].

The application of an external magnetic field H_z in the $+z$ direction can change the magnetization states because $+H_z$ energetically prefers the up domains, leading them to expand. Such expansions of the up domains are accompanied by motion in the domain walls as is well known: a nonzero perpendicular magnetic field induces domain wall motion in PMA films [33,34]. To stop this domain wall

motion, this external H_z should be cancelled at the domain wall by the dipolar field of the magnetization pattern.

III. STRIPE DOMAIN AND MAGNETIZATION

Now we consider the generation of this cancellation field. The cancellation field can be generated by the dipolar field of the up and down domains. To simplify this problem, we change the continuous magnetization model into a discrete model. A cross section of simplified stripe domains is shown in Fig. 1(b) in which the domains and domain walls are replaced with bar magnets. The width of the domain wall bar magnet is $\pi\Delta$ because the integration of $\cosh^{-1}(x/\Delta)$ from $-\infty$ to $+\infty$ yields $\pi\Delta$. At the center of a domain wall [dashed green line in Fig. 1(b)], the up- and down-domain bar magnets generate dipolar fields [$h_{\text{dip,domain}}$, green arrows in Fig. 1(b)] in the z direction. The dipolar fields of individual up and down bar magnets have opposite signs and will cancel each other out, so the remaining dipolar field ($H_{\text{dip,domain}}$) at the domain wall center is due to the excess of up-domain bar magnets over down-domain bar magnets (caused by the energetic preference for $+z$ magnetization created by H_z). It can, therefore, be expressed as the sum of the dipolar fields generated by an array of these uncompensated $+z$ bar magnets of width λ–$2W$ [Fig. 1(b), bottom]. In addition to $H_{\text{dip,domain}}$, the array of domain walls generates a dipolar field [$h_{\text{dip,wall}}$, green arrows in Fig. 1(c)] that prefer $W = \lambda/2$.

After some calculations (see Appendix A), we obtain the following equation at the center of the domain wall.

$$\mu_0 M_S = \frac{2\lambda}{\pi d} \frac{H_z}{R} \bigg/ \left[\sec^2\left(\frac{\pi^2 \Delta}{2\lambda}\right) + \frac{\pi^4}{2}\left(\frac{\Delta \sin\psi}{\lambda}\right)^2 \right]$$
$$\text{(for } \psi \neq 0, N \to \infty, L/\lambda \to \infty\text{)}. \quad (4)$$

Here, M_S is the saturation magnetization and the unit is A/m, $\mu_0 = 4\pi \times 10^{-7}$ T m/A, and H_z is the perpendicular magnetic field and the unit is T. In addition, in typical PMA films, Δ (approximately 10 nm) is much smaller than $\lambda (\gtrsim 200$ nm) [15–17]. Thus, the simplest equation is

$$\mu_0 M_S = \frac{2\lambda}{\pi d} \frac{H_z}{R} \text{ (for } N \to \infty, L/\lambda \to \infty, \Delta/\lambda \to 0\text{)}. \quad (5)$$

Here, R is $(\lambda$–$2W)/\lambda$. R represents a normalized area of the uncompensated domain; $R = +1$ ($W = 0$) means a uniform magnetization state in the $+z$ direction while $R = -1$ ($W = \lambda$) means a uniform magnetization state in the $-z$ direction. It is notable that the original form of Eq. (5) can be found in previous studies [13,14,20–23]. However, these previous results use many normalized variables that hide the important meaning of Eq. (5), which is that imaging techniques can measure the absolute value

of the magnetization because the techniques are already appropriate for measuring λ and R.

It is also important that Eq. (5) implies that the problem of measuring magnetization can be converted into measuring two fundamental values in the International System of Units (SI) [37]. If we use a well-defined coil structure without a magnetic core to generate the magnetic field, then only the geometry information of the coil (defined with lengths) and the electric current in the coil determine the magnetic field. As a result, only two fundamental values of SI base units (ampere and meter) are required for measuring M_S. This differs from previous measurements such as the VSM and the SQUID that require calibration with a reference sample.

IV. APPLICATION LIMIT OF M_S MEASUREMENT

We check the dependence of $H_{\text{dip,domain}}$ on the sample size because real samples are not infinite, unlike our model ($N, L/\lambda \rightarrow \infty$). Figure 1(d) presents the normalized $H_{\text{dip,domain}}$ at the wall center obtained as a function of N and L [see Eqs. (A1) and (A2) in Appendix A]. When $L/\lambda = N = 6$, the stripe domain structure generates 90% of $H_{\text{dip,domain}}(N, L/\lambda \rightarrow \infty)$. To generate 95% of the field, the values of L/λ and N should be 12; for 98%, both values should be 29.

We confirm these predictions by numerical simulations using MUMAX3 micromagnetic software [38]. By using the periodic boundary conditions (PBC), λ is fixed (=1000 nm) (see Appendix B). The change in $(\lambda - 2W)/\lambda$ (=R) with respect to H_z is presented in Fig. 1(e). The simulated graph is linear where $|(\lambda - 2W)/\lambda| < 0.2$, and from the linear relation we can obtain the slope (S): $S = R/H_z$. This slope is in accordance with Eq. (5). Note that Eq. (5) explains only the first-order dependence of R and H_z, but Eq. (A11) in Appendix A includes the higher-order terms.
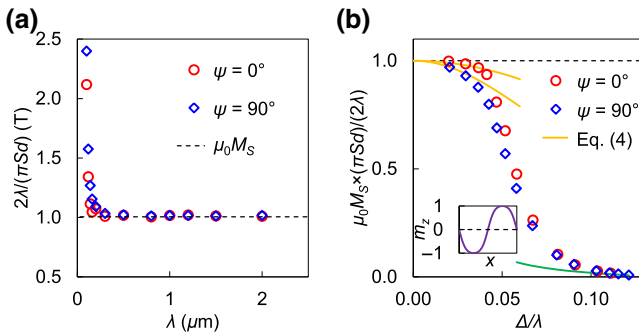

FIG. 2. Simulation results for the expected M_S. (a) $2\lambda/(\pi S d)$ as a function of λ. $\mu_0 M_S$ is depicted as a dashed line. (b) Normalized S as a function of Δ/λ. λ is fixed to 100 nm and A is varied to obtain different Δ values. The inset shows m_z over one period of the stripe pattern with $\Delta/\lambda = 0.1$. The green line represents the simple model of sine function m_z.

The simulation results for the expected M_S as a function of λ are shown in Fig. 2(a) (see Appendix B). When $\lambda \geq 300$ nm, the ratio $2\lambda/(\pi S d)$ obtained from the simulation result matches the value of $\mu_0 M_S$ predicted by Eq. (5). If λ is small (≤ 200 nm), there is a large difference between $2\lambda/(\pi S d)$ and $\mu_0 M_S$. Figure 2(b) shows the normalized value of S as a function of Δ/λ, when $\lambda = 100$ nm. The exchange stiffness constant A is varied from 0.2×10^{-11} to 14.0×10^{-11} J/m to obtain various Δ values. To measure the Δ values, we fit Eq. (3) to m_z. When Δ/λ is small (<0.03), Eq. (4) describes the simulation results well (orange lines). However, when Δ/λ increases, S decreases significantly. This means that there is an additional strong stabilizing force, which is mainly generated by the exchange interaction. The inset of Fig. 2(b) shows m_z as a function of x for one period of the stripe of $\Delta/\lambda = 0.1$. We see that m_z is similar to $m_z(x) = -\sin[\pi x/W]$ for $0 \leq x \leq W$ and $m_z(x) = +\sin[\pi(x-W)/(\lambda-W)]$ for $W \leq x \leq \lambda$. This assumption leads to $S \approx (\lambda^2 M_S)/(4\pi^3 A)$, and this S is represented by the green line in Fig. 2(b).

V. PARALLEL STRIPE DOMAIN BY ELECTRICAL CURRENT AND MOKE MEASUREMENT

We confirm our predictions experimentally using a magneto-optical-Kerr-effect (MOKE) microscope [24]. MOKE microscopes are suitable for applying Eq. (5) experimentally because the spatial resolution is limited to approximately 500 nm. We fabricate $\text{Sub}/\text{Ta}/\text{Pt}/\text{Co}_{40}\text{Fe}_{40}\text{B}_{20}/\text{MgO}/\text{Ta}$ PMA thin films with electrodes (see Appendix C). Without the electric current, the sample shows a random labyrinthine domain configuration [Fig. 3(a)] at zero H_z. Such a labyrinthine state can be changed to the parallel stripe state [Figs. 3(b) and 3(c)] by applying an electric current, because the parallel stripe configuration originates from minimizing the spin torques [15,39,40]. The parallel stripe formation is not easy for a material with strong perpendicular magnetic anisotropy. But the enhancement of the spin torque is favored in the area of magnetization switching and domain wall motion, which results in easier formation of the stripe domain. Such a parallel stripe configuration should be described well by our simple stripe domain model and is, therefore, useful for showing the change in W depending on H_z. The current exerts a force that tilts the domain magnetization from the z axis [34], in deviation from our model, and such tilting reduces $H_{\text{dip,domain}}$. However, the expected tilting (approximately 1°) is sufficiently small that it can be ignored. From the images, we measure W and λ as a function of H_z. Figure 3(d) plots R [=$(\lambda-2W)/\lambda$] vs H_z to find S. We fit the data within the range $|(\lambda-2W)/\lambda| < 0.2$ and obtain $S = 4.23 \pm 0.08$ mT^{-1}. This graph is almost the same as a normalized hysteresis curve. Figure 3(e) plots the variation in λ with H_z, and shows an almost constant
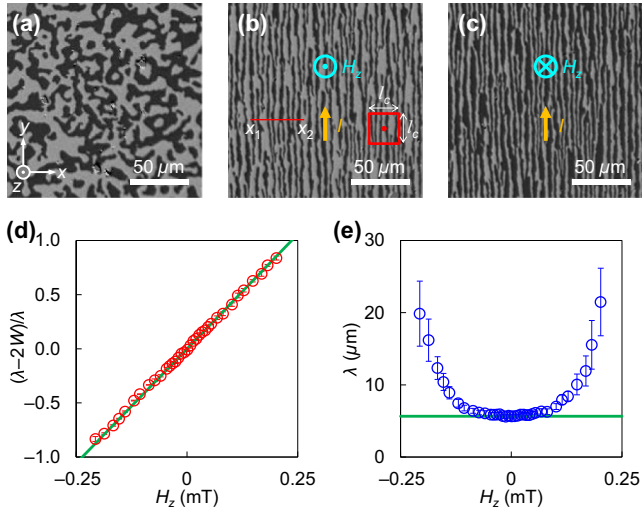
FIG. 3. MOKE image of stripe domains. The sample is $Si-$ $(SiO)_2-Ta$ (3 nm)$-Pt$ (3 nm)$-Co_{40}Fe_{40}B_{20}$ (0.8 nm)$-MgO$ (1.5 nm)$-Ta$ (2 nm) PMA film. (a) Demagnetization state with $H_z = 0$. Light (dark) gray represents up (down) magnetization. (b),(c) Demagnetization states with nonzero H_z and nonzero electric current (I). $|H_z| = 0.04$ mT and $I = 0.11$ A. Assuming that the current does not flow into the MgO layer but flows uniformly to the rest of the layer, the current density is 4.2×10^9 A/m². (d) $(\lambda-2W)/\lambda$ ($=R$) with respect to H_z. The green line is a linear fit. (e) λ as a function of H_z. The green line represents $\lambda = 5.65$ μm. The error bars are obtained from the entire image.

λ ($=5.65 \pm 0.12$ μm) where $|H_z| < 0.02$ mT. Therefore, the obtained M_S is 0.85 ± 0.04 MA/m, which is similar to that of the $Pt-Co_{40}Fe_{40}B_{20}-MgO$ structure (0.9 MA/m) measured by VSM [17,31].

VI. EXPERIMENTS AND IMAGE PROCESSES

Here, we explain some tips for the experiments. First of all, the magnetization image should be captured in the local energy minimum state (or stabilized state) for each H_z value. Applying a constant H_z will eventually result in a stabilized state, but may take a relatively long time. To reduce the time of the experiments, we can quickly change the magnetization state by applying an additional oscillating magnetic field of small amplitude.

After capturing the magnetic image, λ can be obtained. The raw magnetic image (**I**) contains intensity data as a matrix with index (i,j), where i and j are the position indices on the x and y axes, respectively. $I_{i,j}$ is the intensity at (i,j). It is easy to measure λ when the current leads to the parallel stripe state because we can fix j and scan $I_{i,j}$ along i to count the number of times the $I_{i,j}$ value is reversed. If no current is available and a randomly mixed stripe state is formed, then λ can be obtained using the Fourier transforms [13] because the randomness has little effect on the overall results [41].

The basic method of determining R is to measure the normalized hysteresis loop for H_z. We know that this is a well-known method of imaging tools [14,23,24], and therefore, most imaging tools are ready to measure the magnetization. The loop signal is obtained from the sum of all intensity data $\sum_{i,j} I_{i,j}$ in the image. If H_z is large enough, the magnetization is in the saturated state in the $+z$ or $-z$ direction, which also results in saturation of the loop signal. Using these saturation values, R can be obtained by normalizing $\sum_{i,j} I_{i,j}$. Because of the effect of a nonzero Δ, a correction factor is required for the value obtained in the loop to be a valid R. However, the correction is negligible when $\lambda \gg 10\Delta$ (see Appendix D). This basic method is useful when the resolution of the imaging tool is not sufficient to distinguish the detailed stripe structure.

When the resolution of the imaging tool is sufficient to observe the detailed magnetization states, it is possible to obtain R from **I** using two intensity images (**I⁺** and **I⁻**). A sufficient H_z can produce **I⁺** and **I⁻**. **I⁺** (**I⁻**) is the intensity data of the uniform $+z$ ($-z$) magnetization. Then, we compare **I** and (**I⁺** + **I⁻**)/2 at each position (i,j) to determine the local value of R: $R_{i,j}$. For example, when $I_{i,j}^+ > I_{i,j}^-$, $I_{i,j} > (I_{i,j}^+ + I_{i,j}^-)/2$, this means $R_{i,j} = +1$ and when $I_{i,j} < (I_{i,j}^+ + I_{i,j}^-)/2$, it means $R_{i,j} = -1$. The average of all $R_{i,j}$ will give the R in Eq. (5).

Although this method is conceptually simple, the actual situation can have some distortion in the raw image due to sample drift and intensity fluctuations in the light source. Among these, the change in the light source intensity over time is more important because the magnetic signal depends directly on the latter. Figure 4(a) shows examples of intensity data (**I⁺**, **I⁻**, and **I**) along the red line in Fig. 3(b). We can see that most values of **I** exceed (**I⁺** + **I⁻**)/2 (black dashed line) and this results in an invalid R value. Assuming that this is due to the intensity of the light source varying with time, a correction factor (η) can be introduced. Simply, this changes **I** to η**I**. Then, a test function (f) can be introduced. This function quantitatively shows how different $I_{i,j}$ is from $I_{i,j}^+$ and $I_{i,j}^-$ in the entire image: $f(\eta) = \sum_{i,j} [(I_{i,j}^+ - \eta I_{i,j})^2 (I_{i,j}^- - \eta I_{i,j})^2]$. The function $f(\eta)$ is always positive and equals 0 only when all $I_{i,j}$ values are equal to either $I_{i,j}^+$ or $I_{i,j}^-$ for all (i, j). If $I_{i,j}$ are far from $I_{i,j}^+$ or $I_{i,j}^-$, $f(\eta)$ increases. Therefore, a suitable η can be found to minimize $f(\eta)$. Figure 4(b) shows $f(\eta)$ as a function of η and the best value of η is indicated by the black arrow. This η also modifies **I** properly [Fig. 4(a), black solid line]. We call this process Method 1 and this method is used in Fig. 3(d).

In some experimental situations, it is impossible to obtain **I⁺** and **I⁻** because a large H_z is not possible. Then, **I**
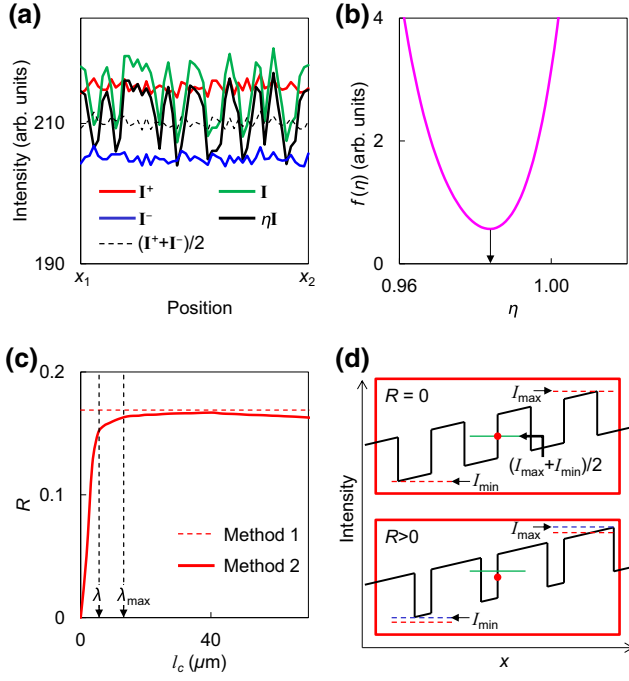
FIG. 4. Image processes. (a) Intensity data of the red line in Fig. 3(b). (b) Values of $f(\eta)$ as a function of η. (c) Obtained R of Fig. 3(b) and comparison between Method 1 and Method 2 with respect to l_c. (d) The effect of the linear slope in intensity. Black lines represent intensity signals. Red dots show the position where local $R_{i,j} = 0$. Red dashed lines represent maximum and minimum values of the intensity in the red boxed area with $R = 0$. Blue dashed lines show the maximum and minimum intensities with $R > 0$. Green lines are the averaged values of maximum and minimum values.

has to get R on its own. In this situation, $I_{i,j}$ should be compared with neighboring data. We call this process Method 2. For example, if we select the position in Fig. 3(b) marked with a red dot, we can cut the red box area to the size of $l_c \times l_c$. The red dot is placed in the center of the box. In this boxed area, the maximum value (I_{max}) and the minimum value (I_{min}) can be found and $(I_{max} + I_{min})/2$ can determine the value of $R_{i,j}$ at the red point. We can expect this method to be valid when $l_c > \lambda$. However, λ varies depending on the location, so a larger l_c is required to obtain the correct R at the position with a larger λ. Therefore, for R to have the correct value in the whole image, l_c has to be larger than the maximum value of the local λ (λ_{max}) [Fig. 4(c)]. An additional increase in l_c from λ_{max} results in noise reduction, which makes the value of R more accurate. The R obtained by Method 2 for $l_c \approx 7\lambda$ is nearly consistent with the value in Method 1. However, any further increase in l_c reduces this consistency. We think this is because the light source intensity varies from position to position in the image. The distribution of this intensity would be a function that varies slowly with

location and generates a background signal in **I**. The effect of an additional linear variation in **I** is shown in Fig. 4(d). The red dots indicate the positions where $R_{i,j}$ is exactly 0. When $R = 0$, the linear slope in **I** causes opposite offsets to I_{max} and I_{min}, and consequently $(I_{max} + I_{min})/2$ does not change. Therefore, $R_{i,j}$ at the red dot becomes 0. However, when $R > 0$, the offsets of I_{max} and I_{min} do not cancel each other in $(I_{max} + I_{min})/2$, and $R_{i,j}$ becomes -1. This will reduce the measured R. When the background intensity has higher-order terms such as x^3, the effect of the background intensity increases with l_c.

VII. CONCLUSION

In conclusion, we show the feasibility of characterizing the absolute value of magnetization of ultrathin PMA films by imaging stripe domains. Magnetic dipolar fields from the magnetic domains are the main origin of stripe formation, and an unequal ratio of up domains to down domains generates an uncompensated dipolar field on the magnetic domain walls. If we apply an external magnetic field to cancel the dipolar field, we can change the ratio of up domains to down domains. In addition, applying an electric current encourages stripe domains parallel to the current direction, which makes it easy to measure the periodicity of the stripes and the stripe width. As a result, we can measure the absolute value of magnetization by the simple observation of domain images. This type of external parameter-induced change in the ratio of stripe patterns could be applied to other physical systems to measure the absolute value of order parameters.

APPENDIX A: DERIVATION OF ANALYTIC EQUATIONS

If we assume that the distance from the domain wall to the uncompensated bar magnet is much larger than λ–$2W$, then the bar magnet can be treated as a line dipole. Therefore, the total dipolar field, $H_{dip,domain}$ (in T), in the z direction at the domain wall center is

$$H_{dip,domain} = -\frac{\pi \mu_0 M_S (\lambda - 2W) d}{2\lambda^2} F\left(N, \frac{L}{\lambda}, \frac{\pi \Delta}{2\lambda}\right),$$

(A1)

$$F(N, l, \delta)$$

$$= \frac{1}{\pi^2} \left[\sum_{n=0}^{(N-1)/2} \frac{l}{(n+1/2-\delta)^2 \sqrt{l^2 + 4(n+1/2-\delta)^2}} \right.$$

$$\left. + \sum_{n=0}^{(N-2)/2} \frac{l}{(n+1/2+\delta)^2 \sqrt{l^2 + 4(n+1/2+\delta)^2}} \right].$$

$$(A2)$$

Here, M_S is the saturation magnetization and $\mu_0 = 4\pi \times 10^{-7}$ T m/A. When $N, l \to \infty$, $F(N, l, \delta) \to \sec^2(\pi\delta)$, so the assumption that the stripe domain pattern continues to infinity in both directions results in

$$H_{\text{dip,domain}} (N, L/\lambda \to \infty)$$

$$= -\frac{\pi\mu_0 M_S(\lambda - 2W)d}{2\lambda^2} \sec^2\left(\frac{\pi^2\Delta}{2\lambda}\right). \quad (A3)$$

Now, we consider $H_{\text{dip,domain}} + H_z = 0$ as the cancellation condition, and then we obtain

$$\mu_0 M_S = \frac{2\lambda}{\pi d} \frac{H_z}{R} / \sec^2\left(\frac{\pi^2\Delta}{2\lambda}\right)$$

$$(\text{for } \psi = 0, N \to \infty, \ L/\lambda \to \infty). \quad (A4)$$

Here, R is $(\lambda - 2W)/\lambda$.

In addition to $H_{\text{dip,domain}}$, the array of domain walls also generates a dipolar field in the x direction. Figure 1(c) shows the dipolar fields (green arrows, $h_{\text{dip,wall}}$) generated by the domain walls. At the center of a certain domain wall (dashed green line), the sum of these dipolar fields generated by the infinite stripes, $H_{\text{dip,wall}}$, can be written as follows using the line dipole assumption ($L/\lambda \to \infty$, $\Delta/\lambda \to 0$)

$$H_{\text{dip,wall}} = \sin\psi \frac{\mu_0 M_S d\Delta}{2}$$

$$\times \left[\sum_{n=1}^{N/2} \left(\frac{1}{(n\lambda + W - \lambda)^2} + \frac{1}{(n\lambda - W)^2} \right) \right.$$

$$\left. - \sum_{n=1}^{(N-1)/2} \frac{2}{(n\lambda)^2} \right]. \quad (A5)$$

Inserting $N \to \infty$ yields

$$H_{\text{dip,wall}} = \sin\psi \frac{\pi^2\mu_0 M_S d\Delta}{2\lambda^2} \left(\csc^2\left(\frac{\pi W}{\lambda}\right) - \frac{1}{3} \right),$$

$$= \sin\psi \frac{\pi^2\mu_0 M_S d\Delta}{2\lambda^2} \left(\sec^2\left(\frac{\pi R}{2}\right) - \frac{1}{3} \right). \quad (A6)$$

Under this $H_{\text{dip,wall}}$, a unit domain wall energy ($e_{\text{dip,wall}}$) as a function of R is

$$e_{\text{dip,wall}} = \pi\Delta d \sin\psi M_S H_{\text{dip,wall}}$$

$$= \sin^2\psi \frac{\pi^3\mu_0 M_S^2 d^2\Delta^2}{2\lambda^2} \left[\sec^2\left(\frac{\pi R}{2}\right) - \frac{1}{3} \right]. \quad (A7)$$

Differentiation of this energy by R gives an effective stabilizing force to make $R = 0$.

$$-\frac{\partial e_{\text{dip,wall}}}{\partial R} = -\left(\frac{\Delta \sin\psi}{\lambda} \right)^2 \frac{\pi^5\mu_0 M_S^2 d^2}{4} R + O(R^3). \quad (A8)$$

We can convert such a stabilizing force into an effective H_z because stabilizing motion always occurs along the x direction likely by H_z-induced domain wall motions. The other energy by H_z is $-M_S H_z d\lambda R = e_{Hz}$ and differentiation by R produces the force induced by H_z.

$$-\frac{\partial e_{Hz}}{\partial R} = -\frac{\partial(-M_S H_z d\lambda R)}{\partial R} = M_S H_z d\lambda. \quad (A9)$$

We can think about the compensation condition of these two forces to stop the wall motion. Taking up to the first order of R in the above two equations gives

$$H_z = \left(\frac{\Delta \sin\psi}{\lambda} \right)^2 \frac{\pi^5\mu_0 M_S d}{4\lambda} R$$

$$= \mu_0 M_S \frac{\pi d}{2\lambda} \left[\frac{\pi^4}{2} \left(\frac{\Delta \sin\psi}{\lambda} \right)^2 \right] R. \quad (A10)$$

This shows the pure contribution of $H_{\text{dip,wall}}$ in Eq. (4). The relative magnitude of this effect compared with that of $H_{\text{dip,domain}}$ is $(\pi^4/2)(\Delta \sin\psi/\lambda)^2$, which modifies Eq. (A4) to Eq. (4). Of course, the energy minimization by using $\partial(e_{\text{dip,domain}} + e_{Hz} + e_{\text{dip,wall}})/\partial R = 0$ with $e_{\text{dip,domain}} = -M_S H_{\text{dip,domain}} d\lambda R$ also yields Eq. (4). Note that if we assume the magnetizations of all domain walls become parallel by applying a sufficient in-plane (x-y plane) magnetic field that reverses the sign of the left-hand side of Eq. (A10), this means $H_{\text{dip,wall}}$ produces a destabilizing force on the domain wall. For example, if we assume that all domain wall magnetization directions are $+x$, $H_{\text{dip,wall}}$ becomes $(\pi^2\mu_0 M_S d\Delta/2\lambda^2)[\sec^2(\pi R/2) + (1/3)]$. As a result, $e_{\text{dip,wall}} = -(\pi^3\mu_0 M_S^2 d^2\Delta^2/2\lambda^2)[\sec^2(\pi R/2) + (1/3)]$ and this reverses the sign of the coefficient of R in Eq. (A10).

It is also notable that Eq. (5) contains only the first-order contribution of R on H_z. This result mainly comes from the line charge assumption. Higher-order terms of R can be

obtained by the integration of $H_{\text{dip,domain}}$ over the x direction because an uncompensated domain has the finite width of $\lambda - 2W$ [Fig. 1(b)]. The result is

$$\mu_0 M_S = \frac{\lambda}{d} \frac{H_z}{\tan(\pi R/2)}$$

$$\text{(for } N \to \infty, L/\lambda \to \infty, \Delta/\lambda \to 0). \quad \text{(A11)}$$

This equation explains the simulation data in Fig. 1(e) (green dots) very well.

APPENDIX B: MICROMAGNETIC SIMULATIONS

We use MUMAX3 micromagnetic software [38]. For Fig. 1(e), the material parameters are: saturation magnetization (M_S), 800×10^3 A/m; exchange stiffness constant (A), 1.5×10^{-11} J/m; perpendicular anisotropy constant (K), 0.8×10^6 J/m^3; thickness (d), 1 nm; structure size (l_x, l_y, l_z), 1000×100 nm$^2 \times d$; cell size for micromagnetic simulation, 2×100 nm$^2 \times d$; repetition numbers for the PBC, (400, 4000, 0). The initial magnetization state is set to half-up and half-down with $\lambda = l_x$ [inset of Fig. 1(e)]. Because of the PBC, λ is fixed to l_x for the duration of the simulation. For Fig. 2(a), λ is imposed by a different l_x. A different ψ can be achieved by setting the interfacial Dzyaloshinskii-Moriya interaction D as 0 (for $\psi = 0°$) or 1 mJ/m^2 (for $\psi = 90°$) [33–35]. For Fig. 2(b), $\lambda = l_x = 100$ nm and A is changed to obtain different values of Δ.

APPENDIX C: SAMPLES AND MOKE MEASUREMENTS

Conventional sputtering systems and photolithography processes are used to produce $Si - (SiO)_2 - Ta$ (3 nm)–Pt (3 nm)–$Co_{40}Fe_{40}B_{20}$ (0.8 nm)–MgO (1.5 nm)–Ta (2 nm) PMA films that are 3-mm wide and 600-μm long. Two Au electrodes are deposited at each end of the magnet to allow the flow of an electric current in the length direction. Figures 3(a)–3(c) show MOKE images. The background image with $-z$ magnetization is subtracted. Light (dark) gray represents $+z$ ($-z$) magnetization.

APPENDIX D: CORRECTION FACTOR FOR R_{LOOP}

The simplest expression of normalized perpendicular magnetization in one period of the stipe is

$$m_z = -\tanh\left(\frac{x}{\Delta}\right) + \tanh\left(\frac{x - W}{\Delta}\right) - \tanh\left(\frac{x - \lambda}{\Delta}\right)$$

$$\text{(for } 0 \leq x \leq \lambda). \quad \text{(D1)}$$

The integration of m_z/λ in $0 \leq x \leq \lambda$ yields R_{loop} (R from the normalized hysteresis loop).

$$R_{\text{loop}} = \frac{1}{\lambda} \int_0^\lambda m_z dx = \frac{\Delta}{\lambda} \ln\left[\cosh\left(\frac{W - \lambda}{\Delta}\right) \text{sech}\left(\frac{W}{\Delta}\right)\right].$$
$$\text{(D2)}$$

The Taylor expansion of R_{loop} near $W = \lambda/2$ with $R = 1 - 2W/\lambda$ results in

$$R_{\text{loop}} = R \tanh\left(\frac{\lambda}{2\Delta}\right) - \frac{R^3}{3}\left(\frac{\lambda}{2\Delta}\right)^2 \text{sech}^2\left(\frac{\lambda}{2\Delta}\right) \tanh$$

$$\times \left(\frac{\lambda}{2\Delta}\right) + \mathcal{O}(R^5). \quad \text{(D3)}$$

When $\lambda/(2\Delta) \to \infty$, $\tanh(\lambda/2\Delta) \to 1$, $(1/3)(\lambda/2\Delta)^2 \text{sech}^2 (\lambda/2\Delta) \tanh(\lambda/2\Delta) \to 0$, and $R_{\text{loop}} \to R$. In detail, when $\lambda = 10\Delta$, $\tanh(\lambda/2\Delta) = 0.99991$ and $(1/3)(\lambda/2\Delta)^2 \text{sech}^2 (\lambda/2\Delta) \tanh(\lambda/2\Delta) = 0.00151$.

[1] R. Mallarino, C. Henegar, M. Mirasierra, M. Manceau, C. Schradin, M. Vallejo, S. Beronja, G. S. Barsh, and H. E. Hoekstra, Developmental mechanisms of stripe patterns in rodents, Nature **539**, 518 (2016).

[2] C. Liu, X. Fu, L. Liu, X. Ren, C. K. Chau, S. Li, L. Xiang, H. Zeng, G. Chen, L. H. Tang, P. Lenz, X. Cui, W. Huang, T. Hwa, and J. D. Huang, Sequential establishment of stripe patterns in an expanding cell population, Science **334**, 238 (2011).

[3] E. Edlund and M. N. Jacobi, Universality of Striped Morphologies, Phys. Rev. Lett. **105**, 137203 (2010).

[4] B. Keimer, S. A. Kivelson, M. R. Norman, S. Uchida, and J. Zaanen, From quantummatter to high-temperature superconductivity in copper oxides, Nature **518**, 179 (2015).

[5] G. Babakhanova, T. Turiv, Y. Guo, M. Hendrikx, Q.-H. Wei, A. P. H. J. Schenning, D. J. Broer, and O. D. Lavrentovich, Liquid crystal elastomer coatings with programmed response of surface profile, Nat. Commun. **9**, 456 (2018).

[6] L. Feigl, P. Yudin, I. Stolichnov, T. Sluka, K. Shapovalov, M. Mtebwa, C. S. Sandu, X.-K. Wei, A. K. Tagantsev, and N. Setter, Controlled stripes of ultrafine ferroelectric domains, Nat. Commun. **5**, 5677 (2014).

[7] D. D. Fong, G. B. Stephenson, S. K. Streiffer, J. A. Eastman, O. Auciello, P. H. Fuoss, and C. Thompson, Ferroelectricity in ultrathin perovskite films, Science **304**, 1650 (2004).

[8] J. Y. Son, S. Song, J.-H. Lee, and H. M. Jang, Anomalous domain periodicity observed in ferroelectric PbTiO$_3$ nanodots having 180° stripe domains, Sci. Rep. **6**, 26644 (2016).

[9] B. Friess, Y. Peng, B. Rosenow, F. von Oppen, V. Umansky, K. von Klitzing, and J. H. Smet, Negative permittivity in bubble and stripe phases, Nat. Phys. **13**, 1124 (2017).

[10] A. A. Koulakov, M. M. Fogler, and B. I. Shklovskii, Charge Density Wave in Two- Dimensional Electron Liquid in Weak Magnetic Field, Phys. Rev. Lett. **76**, 499 (1996).

[11] N. Romming, C. Hanneken, M. Menzel, J. E. Bickel, B. Wolter, K. von Bergmann, A. Kubetzka, and R. Wiesendanger, Writing and deleting single magnetic skyrmions, Science **341**, 636 (2013).

[12] V. Kamberský, P. de Haan, J. Šimšová, S. Porthun, R. Gemperle, and J. C. Lodder, Domain wall theory and exchange stiffness in Co/Pd multilayers, J. Magn. Magn. Mater. **157-158**, 301 (1996).

[13] I. Lemesh, F. Büttner, and G. S. D. Beach, Accurate model of the stripe domain phase of perpendicularly magnetized multilayers, Phys. Rev B **95**, 174423 (2017).

[14] T. H. Johansen, A. V. Pan, and Y. M. Galperin, Exact asymptotic behavior of magnetic stripe domain arrays, Phys. Rev B **87**, 060402 (2013).

[15] W. Jiang, G. Chen, K. Liu, J. Zang, S. G. E. te Velthuis, and A. Hoffmann, Skyrmions in magnetic multilayers, Phys. Rep. **704**, 1 (2017).

[16] S. Woo, Kai Litzius, Benjamin Krüger, Mi-Young Im, Lucas Caretta, Kornel Richter, Maxwell Mann, Andrea Krone, Robert M. Reeve, Markus Weigand, Parnika Agrawal, Ivan Lemesh, Mohamad-Assaad Mawass, Peter Fischer, Mathias Kläui, and Geoffrey S. D. Beach, Observation of room-temperature magnetic skyrmions and their current-driven dynamics in ultrathin metallic ferromagnets, Nat. Mater. **15**, 501 (2016).

[17] S. Woo, Kyung Mee Song, Hee-Sung Han, Min-Seung Jung, Mi-Young Im, Ki-Suk Lee, Kun Soo Song, Peter Fischer, Jung-Il Hong, Jun Woo Choi, Byoung-Chul Min, Hyun Cheol Koo, and Joonyeon Chang, Chang, Spin-orbit torque-driven skyrmion dynamics revealed by time-resolved X-ray microscopy, Nat. Commun. **8**, 15573 (2017).

[18] C. Kooy and U. Enz, Experimental and theoretical study of the domain configuration in thin layers of $BaFe_{12}O_{19}$, Philips Res. Repts **15**, 7 (1960).

[19] D. Craik, *Magnetism: Principles and Applications* (Wiley, New York, 1995).

[20] A. B. Kashuba and V. L. Pokrovsky, Stripe domain structures in a thin ferromagnetic film, Phys. Rev. B **48**, 10335 (1993).

[21] D. Clarke, O. A. Tretiakov, and O. Tchernyshyov, Stripes in thin ferromagnetic films with out-of-plane anisotropy, Phys. Rev. B **75**, 174433 (2007).

[22] N. Saratz, U. Ramsperger, A. Vindigni, and D. Pescia, Irreversibility, reversibility, and thermal equilibrium in domain patterns of Fe films with perpendicular magnetization, Phys. Rev. B **82**, 184416 (2010).

[23] N. Saratz, D. A. Zanin, U. Ramsperger, S. Cannas, D. Pescia, and A. Vindigni, Critical exponents and scaling invariance in the absence of a critical point, Nat. Commun. **7**, 13611 (2016).

[24] J. McCord, Progress in magnetic domain observation by advanced magneto-optical microscopy, J. Phys. D: Appl. Phys. **48**, 333001 (2015).

[25] R. Yamaguchi, K. Terashima, K. Fukumoto, Y. Takada, M. Kotsugi, Y. Miyata, K. Mima, S. Komori, S. Itoda, Y. Nakatsu, M. Yano, N. Miyamoto, T. Nakamura, T. Kinoshita, Y. Watanabe, A. Manabe, S. Suga, and S. Imada, An XMCD-PEEM study on magnetized Dy-doped Nd−Fe−B permanent magnets, IBM J. Res. & Dev **55**, 12 (2011).

[26] P. Fischer, T. Eimüllery, G. Schützz, P. Guttmannx, G. Schmahlx, K. Prueglk, and G. Bayreutherk, Imaging of magnetic domains by transmission x-ray microscopy, J. Phys. D: Appl. Phys. **31**, 649 (1998).

[27] G. Chen, T. Ma, A. T. N'Diaye, H. Kwon, C. Won, Y. Wu, and A. K. Schmid, Tailoring the chirality of magnetic domain walls by interface engineering, Nat. Commun. **4**, 2671 (2013).

[28] E. C. Corredor, S. Kuhrau, F. Kloodt-Twesten, R. Frömter, and H. P. Oepen, SEMPA investigation of the Dzyaloshinskii-Moriya interaction in the single, ideally grown Co/Pt(111) interface, Phys. Rev. B **96**, 060410 (2017).

[29] P. J. A. Van Schendel, H. J. Hug, B. Stiefel, S. Martin, and H.-J. A. Güntherodt, Method for the calibration of magnetic force microscopy tips, J. Appl. Phys. **88**, 435 (2000).

[30] S. Heinze, K. von Bergmann, M. Menzel, J. Brede, A. Kubetzka, R. Wiesendanger, G. Bihlmayer, and S. Blügel, Spontaneous atomic-scale magnetic skyrmion lattice in two dimensions, Nat. Phys. **7**, 713 (2011).

[31] S. Foner, Versatile and sensitive vibrating-sample magnetometer, Rev. Sci. Instrum. **30**, 548 (1959).

[32] M. Aprili, The nanoSQUID makes its debut, Nat. Nanotech. **1**, 15 (2006).

[33] S.-G. Je, D.-H. Kim, S.-C. Yoo, B.-C. Min, K.-J. Lee, and S.-B. Choe, Asymmetric magnetic domain-wall motion by the Dzyaloshinskii-Moriya interaction, Phys. Rev. B **88**, 214401 (2013).

[34] J. Yu, X. Qiu, Y. Wu, J. Yoon, P. Deorani, J. M. Besbas, A. Manchon, and H. Yang, Spin orbit torques and Dzyaloshinskii-Moriya interaction in dual-interfaced Co-Ni multilayers, Sci. Rep. **6**, 32629 (2016).

[35] I. E. Dzyaloshinskii, Thermodynamic theory of weak ferromagnetism in antiferromagnetic substances, Sov. Phys. JETP **5**, 1259 (1957).

[36] T. Moriya, Anisotropic superexchange interaction and weak ferromagnetism, Phys. Rev. **120**, 91 (1960).

[37] B. N. Taylor and A. Thompson, *The International System of Units (SI)*, US Government Printing Office, Gaithersburg, MD, 2008.

[38] A. Vansteenkiste, J. Leliaert, and M. Dvornik, The design and verification of MuMax3, AIP Adv. **4**, 107133 (2014).

[39] K.-W. Moon, C. Kim, J. Yoon, J. W. Choi, D.-O. Kim, K. M. Song, D. Kim, B. S. Chun, and C. Hwang, A spin torque meter with magnetic facet domains, Nat. Commun. **9**, 3788 (2018).

[40] K.-W. Moon, J. W. Choi, C. Kim, J. Yoon, D.-O. Kim, K. M. Song, B. S. Chun, D. Kim, and C. Hwang, Triangular and Sawtooth Magnetic Domains in Measuring the Dzyaloshinskii-Moriya Interaction, Phys. Rev. Appl. **10**, 064014 (2018).

[41] N. Saratz, A. Lichtenberger, O. Portmann, U. Ramsperger, A. Vindigni, and D. Pescia, Experimental Phase Diagram of Perpendicularly Magnetized Ultrathin Ferromagnetic Films, Phys. Rev. Lett. **104**, 077203 (2010).